DESIGN AND IMPLEMENTATION OF A REAL TIME ATTITUDE ESTIMATION SYSTEM WITH LOW COST SENSORS

Roney D. da Silva,* Heloise Assis Fazzolari,* Diego Paolo Ferruzzo Correa*

* *Universidade Federal do ABC, Centro de Engenharia, Modelagem e Ciências Sociais Aplicadas (CECS)*
Santo André, Brazil.

Emails: roney.d@ufabc.edu.br, heloise.fazzolari@ufabc.edu.br, diego.ferruzzo@ufabc.edu.br

Abstract— Getting the attitude of drones, underwater vehicles or other six degree of freedom (DoF) devices is one of the most challenging tasks in the project of navigation control systems. For this reason, many projects use proprietary software or are limited to simulations. This work presents a complete system for attitude determination capable of provide estimated attitude and calibrated measurements using MEMS, with a low-cost and low-power microcontroller. The accelerometer and magnetometer are calibrated online on the embedded system using least squares method without any external devices. The states estimation is computed with a fast algebraic quaternion algorithm (less than 1.5s) using an additive linear Kalman Filter and model measurements.

Keywords— Inertial Sensors, ESP32, MPU-9250, Attitude, Strapdown platform

1 Introduction

One of the biggest challenges when implementing a closed-loop control law is to estimate the system states with precision. Frequently this task could be even more complex than the control itself. In mechanical applications, the states that define the body orientation with respect to a reference system are essential for any control system project. In most cases, the system orientation is described by the Euler's angles. For example, in aeronautics (Castillo et al., 2005; Voos, 2006; Oliveira et al., 2020), quite often the controlled systems is described using six degree of freedom (DoF), three translational and three rotational. Typically, the translational DoF are solved using GPS data, however, the rotational DoF, most of time, requires inertial sensors information, and in some cases another sensor, like optical, ultrasonic or video cameras (Kim et al., 2009; Spinka et al., 2007).

Inertial sensors, which in the past were mostly mechanical, complex and expensive, nowadays are cheaper, smaller and faster. The microelectromechanical systems (MEMS) technology have made the inertial data acquisition become more available at increasingly cheaper prices and also low-weight, low-power consumption and with simple functionality. Today, MEMS are present in many consumer devices, like drones, video games, smartphones and others, and are usually available in modules with three axes magnetometer, gyroscope and accelerometer. This module set is usually known as MARG (magnetic, angular rate and gravity) (Sabatini, 2006). The main drawback of these sensors is the noisy and time-varying biased data they produce. However, most of the literature related to MARG sensors is devoted to address these issues, mainly because the massive range of MEMS inertial sensor applications. Different from the mechanical devices, the MEMS sensors compensate the errors with computational operations. The process to obtain the corrected data, given an specified tolerance and precision, from the sensors output along with a known reference is called calibration. Once calibrations is completed, the next step the attitude calculation.

This work proposes a complete open source, low-cost and low-power platform for attitude determination with focusing on dynamic systems research centers.

This paper is structured as follows: Sections 2.1.1 to 2.1.3 introduce briefly the calibrations methods for each sensor. Section 2.2 show the AQUA algorithm to obtain the measurement model from accelerometer and magnetometer. The sensor fusion with the Kalman filter is presented in section 2.3. The experimental results of calibrations and estimation are in the section 3. Section 4 contains the concluding remarks.

2 Methodology

2.1 Calibration Methods

Each of the MARG sensors can have its measurements degraded by particular factors, however, the common errors are (Titterton and Weston, 2004):

- Bias: constant signal with low changes, often different in each initialization;
- Scale factor: commonly considered as a linear value proportional to the input;
- Misalignment: due to the assembly;
- Thermal drift: additional value occasioned by temperature changes; and

- Quantization: white noise added by the discretization, usually proportional to the quantization.

Titterton and Weston (2004) define an integrated inertial sensors system with a dedicated computer, assembled in a fixed base coinciding with a body base as a strapdown platform. This configuration is used for testing the calibration methods and for attitude determination, mainly because the body dynamics can be neglected (Groves, 2015). It is well-know that each sensor has a particular calibration procedure, however, roughly speaking, it can be said that all of them use the same principle: a reference field vector, which allows to: a) explore the fact that the sum of the square triaxial sensor output is equal to the reference vector inner product; b) directly compare the reference vector to sensors output. For example: the accelerometer is a sensor that measures a specific force, if it is possible to rotate the platform without adding translational acceleration, the approach a) can be used. If the strapdown platform has a parallelepiped shape, it is possible to found a normal plane to the gravity field for collecting data in a static position, so the principle b) can be used.

The principle a), explored in several works, has as main difficulty the solution of nonlinear equations. In the literature, this disadvantage is addressed using iterative methods (Frosio et al., 2009; Won and Golnaraghi, 2010) and nonlinear optimization algorithms (Kuncar et al., 2017). In this sense, Zhong et al. (2018) compute the calibration parameters applying a damped Gauss-Newton algorithm called Levenberg-Marquardt , reducing the noise in the measures using a smoothing filter. The approach b) provides more information because of the usage of a vector instead of its norm, considering the misalignment between the body and the MARG axes (Kuncar et al., 2016).

In order to apply the same concepts to the magnetometer, the magnitude of the magnetic vector field as well the inclination value are both needed, this information could be found on the internet[1]. However, aligning each of the axis to the direction of the local magnetic field is not an easy task and furthermore, it requires additional equipment. Therefore, the approach a) is more common in the literature, the standard procedure, found in many works, uses measurements collected during full rotations, which exposes each axis to maximum and minimum values, therewith, scale factor and biases can be estimated (Kuncar et al., 2016), non-orthogonality can also be considered in the computations (Merayo et al., 2000; Bonnet et al., 2009; Schiffler et al., 2014).

Due to the limited computational capacity inherent to the embedded systems, the simplifications made in the project are important for the succeed of the implementation. In this sense, special attention has to be pay to the non-orthogonality nature of the homogeneous equation that needs to be solved either using singular values decomposition (Schiffler et al., 2014; Bonnet et al., 2009), adjusted least squares estimation (Merayo et al., 2000; Markovsky et al., 2004), or eigenvector solution (Pedley and Stanley, 2014). The experimental results show that the simplified model presented in the section 2.1.3 is sufficiently accurate for the purpose of this work.

[1]National Geophysical Data Center on website www.ngdc.noaa.gov/geomag/calculators/magcalc.shtml

2.1.1 Accelerometer:

The method proposed by Kuncar et al. (2016), consider misalignment between the global and body systems, scale factor and bias, respectively modeled by matrices $\mathbf{M}_d \in \mathbb{R}^{3\times3}$, $\mathbf{M}_{FS} \in \mathbb{R}^{3\times3}$ and $\mathbf{b} \in \mathbb{R}^3$. Arranging the three component of the accelerometer into the $\mathbb{R}^3$ vector $\boldsymbol{a}_m = \begin{bmatrix} a_x & a_y & a_z \end{bmatrix}^\intercal$, the relationship between compensate acceleration $\boldsymbol{a}_c$ with the MARG measurements is given by:

$$\boldsymbol{a}_c = \mathbf{M}_d\,\mathbf{M}_{FS}\left[\boldsymbol{a}_m - \mathbf{b}\right] \tag{1}$$

For convenience is set $\mathbb{R}^{3\times3}$ matrix $\mathbf{M} = \mathbf{M}_d\,\mathbf{M}_{FS}$ and $\mathbb{R}^3$ vector $\boldsymbol{a}_{offset} = -\mathbf{M}_d\,\mathbf{M}_{FS}\mathbf{b}$, then Eq. (1) can be rewrite like Eq. (2):

$$\boldsymbol{a}_c = \mathbf{M}\boldsymbol{a}_m + \boldsymbol{a}_{offset} \tag{2}$$

The accelerometer calibration consist in finding 12 parameters (nine of $\mathbf{M}$ matrix and three of the offset vector $\boldsymbol{a}_{offset}$). The Eq. (2) can be appropriately rewritten as:

$$\boldsymbol{a}_c^\intercal = \begin{bmatrix} \boldsymbol{a}_m^\intercal & 1 \end{bmatrix} \begin{bmatrix} \mathbf{M}^\intercal \\ \boldsymbol{a}_{offset}^\intercal \end{bmatrix} \tag{3}$$

In an ideal scenario, with the MARG module steady and one of the axes pointing downward, on the gravity direction, for example, x-axes down, Eq. (3) should read

$$\begin{bmatrix} 9.81 & 0 & 0 \end{bmatrix} = \begin{bmatrix} \boldsymbol{a}_m^\intercal & 1 \end{bmatrix} \begin{bmatrix} \mathbf{M}^\intercal \\ \boldsymbol{a}_{offset}^\intercal \end{bmatrix} \tag{4}$$

and, y-axes up, the Eq. (3) is:

$$\begin{bmatrix} 0 & -9.81 & 0 \end{bmatrix} = \begin{bmatrix} \boldsymbol{a}_m^\intercal & 1 \end{bmatrix} \begin{bmatrix} \mathbf{M}^\intercal \\ \boldsymbol{a}_{offset}^\intercal \end{bmatrix} \tag{5}$$

It is possible to compute the calibration parameters proceeding similarly with the other axes, collecting N non-calibrated accelerometer measurements and arranged the i-th measurements on i-th row of matrix $\mathbf{W} \in \mathbf{R}^{N\times4}$ like $\begin{bmatrix} a_x & a_y & a_z & 1 \end{bmatrix}$, and simultaneously, each row of the matrix $\mathbf{Y} \in \mathbf{R}^{N\times3}$ are completed with corrected value that sensor should present. With N samples, the system are formed:

$$\mathbf{Y}_{N\times3} = \mathbf{W}_{N\times4} \begin{bmatrix} \mathbf{M}^\intercal \\ \boldsymbol{a}_{offset}^\intercal \end{bmatrix}_{4\times3} \tag{6}$$

The parameters are then obtained using the last squared method by solving Eq. (7)

$$\begin{bmatrix} \mathbf{M}^\intercal \\ \boldsymbol{a}_{offset}^\intercal \end{bmatrix} = (\mathbf{W}^\intercal \mathbf{W})^{-1} \mathbf{W}^\intercal \mathbf{Y} \tag{7}$$

2.1.2 Gyroscope

The gyroscope measures angular rate, then for a precise calibration is required a device that provides know rotations, thus, the calibration method introduced insection 2.1.1 can be applied and the calibration parameters can be found. If the nonlinearity and misalignment are neglected, a practical solution can be found by compensating only the systematic error as follows:

$$\mathbf{b}_{giro} = \frac{\sum_{i=0}^{N} \boldsymbol{\omega}_m}{N \times f_{giro}} \tag{8}$$

where f_{giro} is the scale factor provided by the manufacturer and N is the number of data samples. The compensated measurements of the gyroscope ${}^b\boldsymbol{\omega}_c$ is given by Eq. (9)

$$\boldsymbol{\omega}_c = f_{giro} \cdot (\boldsymbol{\omega}_m - \mathbf{b}_{giro}) \tag{9}$$

2.1.3 Magnetometer:

The magnetometer generally is used to measure magnetic field direction of Earth. So, for the attitude, the additional magnetic influence can be eliminated from magnetometer output, given by vector $\mathbf{m}_m \in \mathbb{R}^3$. Considering an attitude matrix $\mathbf{R} \in \mathbb{R}^{3\times3}$, the relationship between measure $\mathbf{m}_m$ and the local Earth magnetic field vector $\mathbf{m}_e \in \mathbb{R}^3$ (Pedley and Stanley, 2014) is given by

$$\mathbf{m}_c = \mathbf{R}\,\mathbf{m_e} \tag{10}$$

Although the same errors present on the accelerometer calibration can be found in magnetometers, there are two particular characteristics called soft-iron and hard-iron that should be consider on the magnetometer calibration method. Soft-iron is an electromagnetic interference generate by elements of the device itself and can be time-dependent. In practical approaches, soft-iron effects change the scale factor. We represent this effects with the matrix $\mathbf{S} \in \mathbb{R}^{3\times3}$. Hard-iron errors are generated by ferromagnetic devices close to the sensor, which may add time invariant constant values to the sensor's output. The hard-iron errors are denoted by the vector $\mathbf{b} \in \mathbb{R}^3$. The magnetometer's measurements degraded by these two interference $\mathbf{m_m}$ can be modeled as Eq. (11)

$$\mathbf{m}_m = \mathbf{S}\mathbf{m}_c + \mathbf{b} \tag{11}$$

where $\mathbf{m}_c = \mathbf{R}\mathbf{m}_e$. With the measurements $\mathbf{m}_m$, we can, by geometric approach, obtain the compensated measurements $\mathbf{m}_c$ – which is the same as $\mathbf{R}\mathbf{m}_e$ – then:

$$\mathbf{R}\mathbf{m}_e = \mathbf{S}^{-1}(\mathbf{m}_m - \mathbf{b}) \tag{12}$$

where $\mathbf{S} = \operatorname{diag}\begin{pmatrix} x_{sf} & y_{sf} & z_{sf} \end{pmatrix}$. Note that $\mathbf{m}_e^\intercal \mathbf{R}^\intercal \mathbf{R}\mathbf{m}_e = \mathbf{m}_e^\intercal \mathbf{m}_e$ represent the module of local magnetic field, which is assumed to be constant.

$$\mathbf{m}_e^\intercal \mathbf{m}_e = (\mathbf{m}_m - \mathbf{b})^\intercal \mathbf{S}^{-\intercal}\mathbf{S}^{-1}(\mathbf{m}_m - \mathbf{b}) \tag{13}$$

Expanding the terms of the Eq. (13) we have:

$$\mathbf{m}_e^\intercal \mathbf{m}_e = \left(\frac{m_x - b_x}{x_{sf}}\right)^2 + \left(\frac{m_y - b_y}{y_{sf}}\right)^2 + \left(\frac{m_z - b_z}{z_{sf}}\right)^2 \tag{14}$$

From the geometric perspective, if we rotate the MARG module, the constant field should generate an ellipsoid. Mathematically this is verified in Eq. (14). In an ideal setting, the surface generated by the rotations should be a perfect sphere with center on origin, but the hard-iron effects shifts the center locus and the soft-iron deforms the perfect sphere into an ellipsoid. The geometric method can be considered as the procedure of the shifted ellipsoid parameterization in a centered sphere with radius R that should be equal to the local magnetic field module. Therefore, the magnetometer calibration consists in estimate the scale factor and bias that make the transformation possible.

$$m_x^2 - 2m_x b_x + b_x^2 + \left(\frac{x_{s_f}}{y_{s_f}}\right)^2 \left(m_y^2 - 2m_y b_y + b_y^2\right) + \left(\frac{x_{s_f}}{z_{s_f}}\right)^2 \left(m_z^2 - 2m_z b_z + b_z^2\right) = x_{s_f}^2 R^2 \tag{15}$$

We can rewrite Eq. (15) on matrix form:

$$m_x^2 = \begin{bmatrix} m_x \\ m_y \\ m_z \\ -m_y^2 \\ -m_z^2 \\ 1 \end{bmatrix}^\intercal \begin{bmatrix} 2b_x \\ 2\left(\frac{x_{s_f}}{y_{s_f}}\right)^2 b_y \\ 2\left(\frac{x_{s_f}}{z_{s_f}}\right)^2 b_z \\ \left(\frac{x_{s_f}}{y_{s_f}}\right)^2 \\ \left(\frac{x_{s_f}}{z_{s_f}}\right)^2 \\ \xi \end{bmatrix} \tag{16}$$

where $\xi = x_{s_f}^2 R^2 - b_x^2 - \left(\frac{x_{s_f}}{y_{s_f}}\right)^2 b_y^2 - \left(\frac{x_{s_f}}{z_{s_f}}\right)^2 b_z^2$. Eq. (16) associates the measurements in linear form, and can be rewrite as

$$\mathbf{w} = \mathbf{H}\mathbf{x} \tag{17}$$

For the i-th measurements of the N samples, ${m_x}^2$ is allocated on i-th vector element $\mathbf{w} \in \mathbb{R}^N$ and simultaneously, $\begin{bmatrix} m_x & m_y & m_z & -m_y^2 & -m_z^2 & 1 \end{bmatrix}$ on i-th matrix row $\mathbf{H} \in \mathbb{R}^{N\times3}$ are function of the magnetometer measurements. The vector $\mathbf{x} \in \mathbb{R}^3$ contain all the parameters that compensate the sensors measurements obtained by the least squared method

$$\mathbf{x} = (\mathbf{H}^\intercal \mathbf{H})^{-1} \mathbf{H}^\intercal \mathbf{w} \tag{18}$$

The vector $\mathbf{x} = [x_0, \ldots, x_5]^\intercal$ is the Eq. (18) solution and makes it possible to obtain the calibration parameters

$$\begin{aligned} b_x &= \frac{x_0}{2} \qquad y_{s_f} = \sqrt{\frac{x_{s_f}^2}{x_3}} \\ b_y &= \frac{x_1}{2 \cdot x_3} \quad z_{s_f} = \sqrt{\frac{x_{s_f}^2}{x_4}} \\ b_y &= \frac{x_2}{2 \cdot x_4} \\ x_{s_f} &= \frac{\sqrt{x_5 + b_x^2 + x_3 b_y^2 + x_4 b_z^2}}{R} \end{aligned} \tag{19}$$

where x_i as i-th component from vector $\mathbf{x}$. The compensated magnetometer data it is obtained with Eqs. (10) and (12).

2.2 Measurement model

In Valenti et al. (2016) is introduced the Algebraic Quaternion Algorithm (AQUA), where the orientation quaternion is obtained algebraically. The body and inertial frames are denoted by b and i respectively. We assume the Earth it is an inertial frame. The ${}^i x$ and ${}^i z$ coinciding with magnetometer north and gravitational direction. The accelerometer, gyroscope and magnetometer measurements are arranged into the ${}^b\boldsymbol{a}$, ${}^b\boldsymbol{\omega}$ and ${}^b\mathbf{m}$

$${}^b\boldsymbol{a} = \begin{bmatrix} a_x & a_y & a_z \end{bmatrix}^\intercal \tag{20a}$$

$${}^b\boldsymbol{\omega} = \begin{bmatrix} \omega_x & \omega_y & \omega_z \end{bmatrix}^\intercal \tag{20b}$$

$${}^b\mathbf{m} = \begin{bmatrix} m_x & m_y & m_z \end{bmatrix}^\intercal \tag{20c}$$

The measurement is a quaternion that is function of the accelerometer and magnetometer reads, denoted in this work as $\mathbf{q}_{obs}$ and is obtained with the quaternion product

$${}^b_i\mathbf{q}_{obs} = {}^b_\Pi\, \mathbf{q}_{accel} \otimes {}^\Pi_i\, \mathbf{q}_{mag} \tag{21}$$

where :

$${}^b_\Pi\mathbf{q}_{acel} = \begin{cases} \frac{\sqrt{2}}{2} \begin{bmatrix} \kappa_1 & -\frac{a_y}{\kappa_1} & \frac{a_x}{\kappa_1} & 0 \end{bmatrix}^\intercal & , a_z \geq 0 \\ \frac{\sqrt{2}}{2} \begin{bmatrix} -\frac{a_y}{\kappa_2} & \kappa_2 & 0 & \frac{a_x}{\kappa_2} \end{bmatrix}^\intercal & , a_z < 0 \end{cases} \tag{22a}$$

and

$$\kappa_1 = \sqrt{1 + a_z} \tag{22b}$$

$$\kappa_2 = \sqrt{1 - a_z} \tag{22c}$$

With the $\mathbf{q}_{accel}$, the magnetometer measurement in body reference is rotated to intermediate frame Π with:

$${}^\Pi\mathbf{l}_q = {}^b_\Pi\, \mathbf{q}_{acel} \otimes {}^b\mathbf{m}_q \otimes {}^b_\Pi\mathbf{q}^*_{acel} \tag{23}$$

where ${}^b\mathbf{m}_q$ the magnetometer measurement write as pure quaternion, then to find the quaternion that rotate the magnetometer in intermediate frame to inertial frame we are using the following system:

$${}^\Pi\mathbf{l}_q = {}^\Pi_i\, \mathbf{q}_{mag} \otimes {}^i\mathbf{l}_q \otimes {}^\Pi_i\mathbf{q}^*_{mag} \tag{24}$$

$\mathbf{q}_{mag}$ rotated from the inertial frame to the intermediate one is given by:

$${}^\Pi_i\mathbf{q}_{mag} = \begin{cases} \frac{\sqrt{2}}{2} \begin{bmatrix} \frac{\beta_1}{\sqrt{\Gamma}} & 0 & 0 & \frac{l_y}{\beta_1} \end{bmatrix}^\intercal & l_x \geq 0 \\ \frac{\sqrt{2}}{2} \begin{bmatrix} \frac{l_y}{\beta_2} & 0 & 0 & \frac{\beta_2}{\sqrt{\Gamma}} \end{bmatrix}^\intercal & l_x < 0 \end{cases} \tag{25a}$$

where $\Gamma = l_x^2 + l_y^2$ and

$$\beta_1 = \sqrt{\Gamma + l_x\sqrt{\Gamma}} \tag{25b}$$

$$\beta_2 = \sqrt{\Gamma - l_x\sqrt{\Gamma}} \tag{25c}$$

2.3 Estimation

It is well known that through integration it is possible to obtain the attitude using the gyroscope measurements exclusively, but as will be see in the results, the angular-rate integral can diverge very quickly. In the literature some practical solutions include sensor fusion, for example, the complementary filters with constant gain presented in (Madgwick et al., 2011) and the adaptive gain in (Valenti et al., 2015), also the well known linear Kalman filter (KF) (Valenti et al., 2016; Guo et al., 2017; Feng et al., 2017) and the extended Kalman filter (EKF) (Sabatini, 2006; Baroni, 2017). Complementary Filters can be computationally more efficient, however, they rely on experimental results for tuning the gains and it can work well only in specific cases. On the other hand, the Kalman filter is an optimal estimator with respect to the minimal mean-squared error. In this section will present the Kalman filter from the perspective of sensor fusion.

With the initial conditions

$$\mathbf{q}^+_{k=0} = \mathbf{q}_0 \tag{26}$$

$$\mathbf{P}^+_{k=0} = \mathbf{P}_0 \tag{27}$$

The quaternion $\mathbf{q}^-_k$ and the covariance matrix of the linear prediction $\mathbf{P}^-_k$ are propagated with the previously estimated quaternion $\mathbf{q}^+_{k-1}$ and the last angular rate from the gyroscope measurement ${}^b\boldsymbol{\omega}_k$. Mathematically,

$$\mathbf{q}^-_k = \mathbf{A}_k \left({}^b\boldsymbol{\omega}_k\right)\, \mathbf{q}^+_{k-1} \tag{28}$$

$$\mathbf{P}^-_k = \mathbf{A}_k \mathbf{P}^+_{k-1} \mathbf{A}^\intercal_k \left({}^b\boldsymbol{\omega}_k\right) + \mathbf{Q}_k \tag{29}$$

$\mathbf{Q}_k$ represent the process noise covariance and $\mathbf{A}_k$ is the transition matrix

$$\mathbf{Q}_k = \left(\frac{\Delta t}{2}\right)^2 \mathbf{G}_k \sum\nolimits_g \mathbf{G}^\intercal_k \tag{30}$$

$$\mathbf{A}_k \left({}^b\boldsymbol{\omega}_k\right) = \mathbb{I}_4 + \frac{\Delta t}{2} \boldsymbol{\Omega} \left({}^b\boldsymbol{\omega}_k\right) \tag{31}$$

To compute process noise covariance it is necessary the covariance matrix $\mathbb{R}^{3\times3}$ $\sum_g$ = diag$\begin{pmatrix} \sigma_x & \sigma_y & \sigma_z \end{pmatrix}$, where σ_x, σ_y and σ_z are standard deviation of the gyroscope axes on body frame. The $\mathbf{G}_k$ and $\mathbf{\Omega}\left({}^b\boldsymbol{\omega}_k\right)$ are

$$\mathbf{G}_k\left(\mathbf{q}_{k-1}^+\right) = \begin{bmatrix} q_1 & q_2 & q_3 \\ -q_0 & q_3 & -q_2 \\ -q_3 & -q_0 & q_1 \\ q_2 & -q_1 & -q_0 \end{bmatrix} \tag{32}$$

$$\mathbf{\Omega}\left({}^b\boldsymbol{\omega}_k\right) = \begin{bmatrix} 0 & \omega_x & \omega_y & \omega_z \\ -\omega_x & 0 & \omega_z & -\omega_y \\ -\omega_y & -\omega_z & 0 & \omega_x \\ -\omega_z & \omega_y & -\omega_x & 0 \end{bmatrix} \tag{33}$$

With the quaternion measurement $\mathbf{q}_{obs_k}\left({}^b\boldsymbol{a}_k, {}^b\mathbf{m}_k\right)$ and covariance matrix measurement $\mathbf{R}_k\left({}^b\boldsymbol{a}_k, {}^b\mathbf{m}_k\right)$, the updating process for the Kalman gain $\mathbf{K}_k$, the estimated state $\mathbf{q}_k^+$ and *a posteriori* covariance matrix $\mathbf{P}_k^+$ is:

$$\mathbf{K}_k = \mathbf{P}_k^-\left(\mathbf{P}_k^- + \mathbf{R}_k\right)^{-1} \tag{34}$$

$$\mathbf{q}_k^+ = \mathbf{q}_k^- + \mathbf{K}_k\left(\mathbf{q}_{obs_k} - \mathbf{q}_k^-\right) \tag{35}$$

$$\mathbf{P}_k^+ = \left(\mathbb{I}_N - \mathbf{K}_k\right)\mathbf{P}_k^- \tag{36}$$

$\mathbf{R}_k$ is the covariance matrix of the additive noise of the measurement. To compute this matrix we need the standard deviation of the accelerometer and the magnetometer measurements and also the Jacobian matrix $J = \frac{\partial \mathbf{q}_{obs}}{\mathbf{u}}$, where $\mathbf{u} = \begin{bmatrix} {}^b\boldsymbol{a} & {}^b\mathbf{m} \end{bmatrix}^\intercal$. This matrix is omitted here but can be consulted in Valenti et al. (2016).

3 Experimental Results

The platform consists of two modules: an open-source microcontroller ESP32 with Tensilica Xtensa LX6 240 MHz with 4 MiB flash memory; nine Dof MARG MPU-9250 — both low-cost and low-power. For telemetry, the ESPNOW protocol was used that support 250 B of payload transfer. The ESPNOW and ESP32 was developed by the Chinese Espressif and the MPU-9250 by InvenSense (InvenSense, 2016; Espressif, 2020). The internal components and the platform itself can be seen in Figs. 1a and 1b respectively. The parallelepiped shape of the platform is essential for calibrating the accelerometer.

3.1 Calibration methods results

In the performance evaluation stage of the calibration methods, the implementation sends uncompensated and compensated MARG data to a PC at 50 Hz. When the actual calibration process starts 100 measurements are collected from six different positions and the procedure presented in sections 2.1.1 and 2.1.2 is applied and the calibration parameters computation take place. In

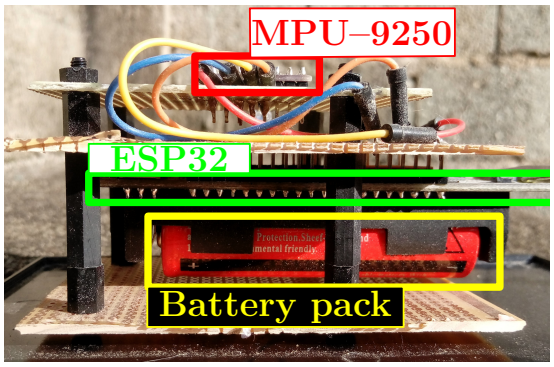

(a) Internal parts

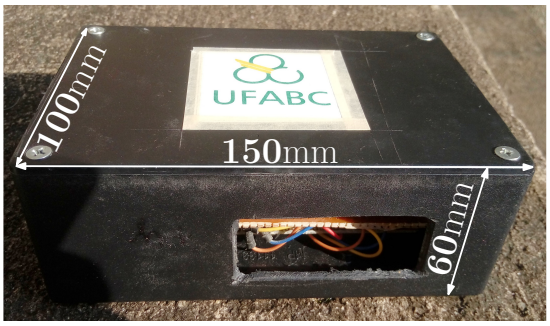

(b) Platform case

Figure 1: Platform used for the experiments. The internal components are shown at the top and the platform itself is shown at the bottom.

a second stage, the platform is rotated around all three axes and 1000 samples are collected, then, the magnetometer calibrated parameters are computed following the procedure described in section 2.1.3. The gravitational and magnetic field used as reference were 9.80 m s^{-2} and $|\mathbf{m}_e|$=22.8968 µT respectively.

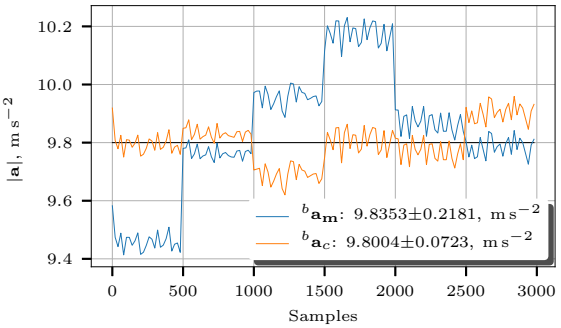

Figure 2: Norm of ${}^b\boldsymbol{a}_m$ and ${}^b\boldsymbol{a}_c$. The gravity reference value is $\mathbf{g} = 9.80\,\mathrm{m\,s^{-2}}$

Fig. 2 shows the accelerations norm ${}^b\boldsymbol{a}_m$ and ${}^b\boldsymbol{a}_c$ for 3000 samples collected with the platform steady in six different positions. The calibration methods keep the ${}^b\boldsymbol{a}_c$ norm very close to the reference and reduces up to 66% the standard deviation with respect to ${}^b\boldsymbol{a}_m$. Fig. 3 shows 600 samples for the three gyroscope axes with platform stopped. Different from the accelerometer,

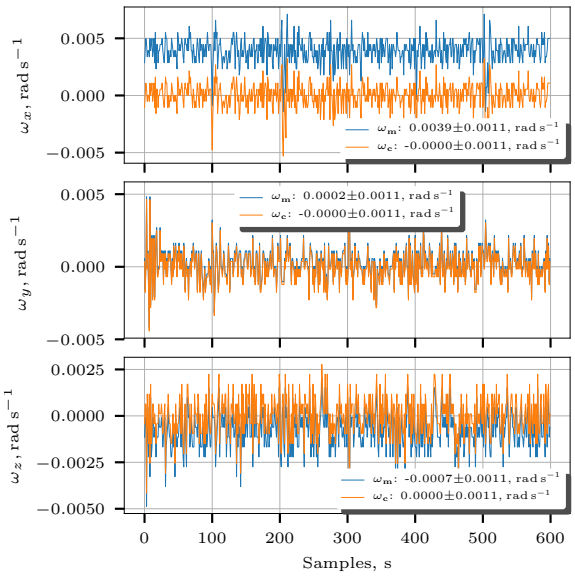

Figure 3: Systematic error compensation results related to the angular velocities ω_x, ω_x and ω_z. The methods does not change the measurements standard deviation.

the calibration method do not affect the standard deviation, but only the measurements mean. To assess the effect of having disregarded the scale factor, an external reference velocity device would be needed. Nevertheless, according to the manufacturer, gyroscope non-linearity is around 0.1%, which is five times smaller than the accelerometer non-linearity. Thus, for typical mechanical device we have good results.

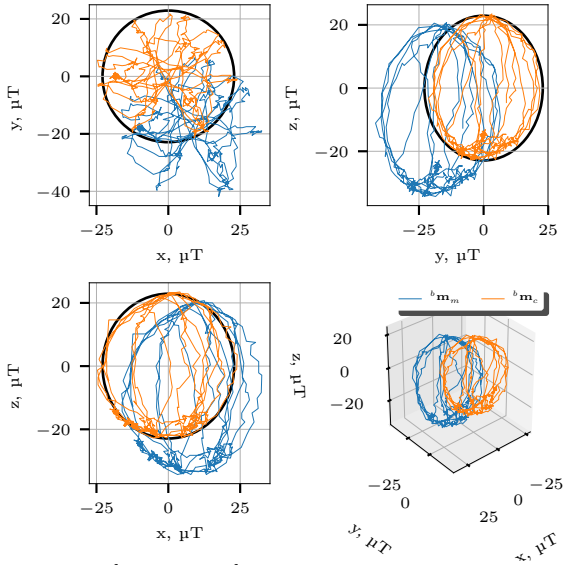

Figure 4: ${}^b\mathbf{m}_m$ and ${}^b\mathbf{m}_c$ measurements from the magnetometer. Misalignment from the reference is shown in blue and deformation is shown in orange.

Fig. 4 show the state space and the three-dimensional representation of the magnetometer measurements. The curves in black on state space representations have radius equal to $|\mathbf{m}_e|$, it can be see that the non-centralized distribution is more significant than the deformation, in other words, the hard-iron interference is more distinguishable than soft-iron influence, given this, it can be said that, disregard the axis misalignment could be an adequate simplification.

3.2 Estimation method results

For the performance evaluation of the online estimator, the platform is manually rotated during 12 s while it sends the nine compensated data of the three MARG sensors, along with four estimated quaternion components, three Euler's angles and the time Δt elapsed since the last data sent. Note that 17 floats amount to 68 B, which represents just 26,67% of maximum payload. Fig. 5 shows the normalized ${}^b\boldsymbol{a}_c$, ${}^b\mathbf{m}_c$, and ${}^b\boldsymbol{\omega}_c$ in rad s^{-1}. The curves smoothness for the accelerometer and the gyroscope, in the first and the third plots, is due to the 20 Hz digital low-pass filter (DLPF), available for these sensors in the MPU-9250.

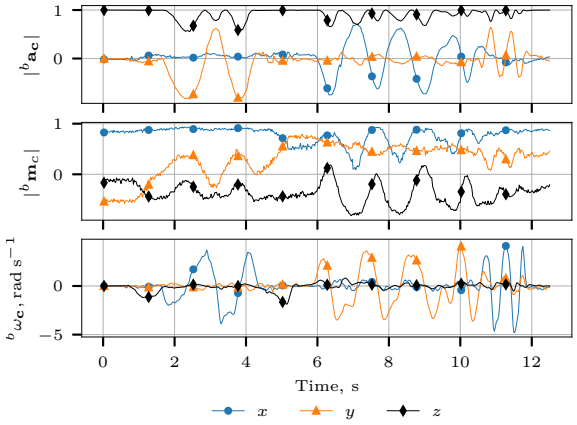

Figure 5: Acceleration, magnetic field and angular rate for the three access, collected from the MARG during the performance evaluation.

With the compensated measurements and Δt aldeary computed, it is possible to construct the four quaternions: $\mathbf{q}_{obs}$ and $\mathbf{q}^-$ obtained from Eqs. (21) and (28), $\mathbf{q}_{giro}$ which results of pure integration with initial condition $\mathbf{q}_{giro}|_{k=0} = \mathbf{q}^+|_{k=0}$, and the estimated quaternion $\mathbf{q}^+$ can be computed using Eq. (35).

Fig. 8 shows the quaternions time evolution. Note that these are online computations, which are obtained and transmitted by the platform in real time.

The Euler's angles shown in Fig. 6 are computed from the quaternions shown in Fig. 8. If the accelerometer and the magnetometer measurements were used exclusively in the computations, we would expect more noisy estimations. Similarly, if just the gyroscope measure-

ment were used, then a fast deviation would be obtained. Sensor fusion with Kalman filter provides a smoother result without deviations. The results obtained seems not to be affected whether float or double variables are used in the computations, nevertheless, the time consumption using double type is ≈2.5 times bigger than when using float type, as shown figure Fig. 7.

The computational implementation uses the open-source Eigen library C++ 3.3.7 and compiled with `-Ofast` (Guennebaud et al., 2010).

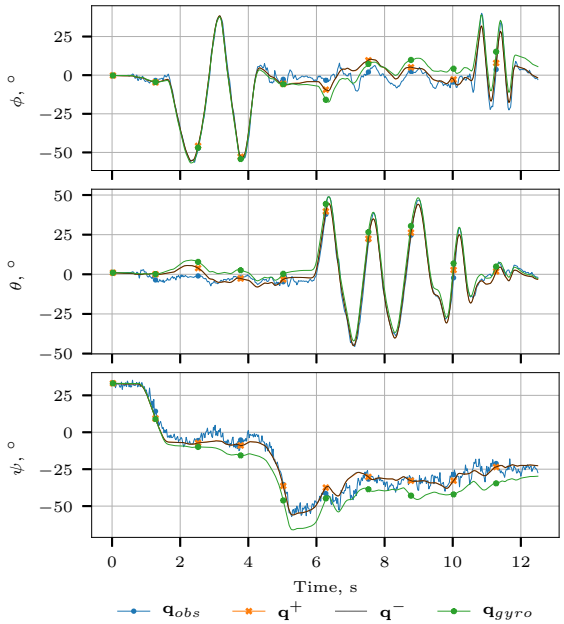

Figure 6: Euler angles extracted from quaternions of the Fig. 8

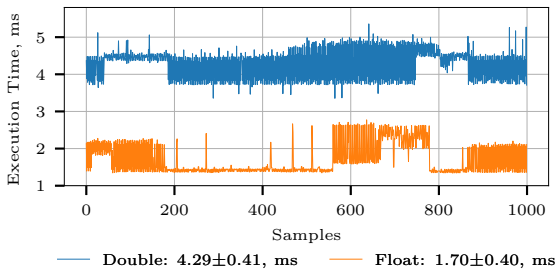

Figure 7: Time consumption with double and float variable type

4 Conclusions

This work shows that is possible to obtain the attitude with a low-cost and low-power microcontroller and a MARG unit. The simplifications on the calibration methods were justified by the good experimental results obtained, given the embedded hardware limitations. The estimation using algebraic quaternion does not require any optimization or iterative methods, providing a fast response in a relative simple project. This contribution provides a tested and easily mounted platform that can be used for research purposes on drones or any another mechanical devices for research on dynamics and control laws implementations.

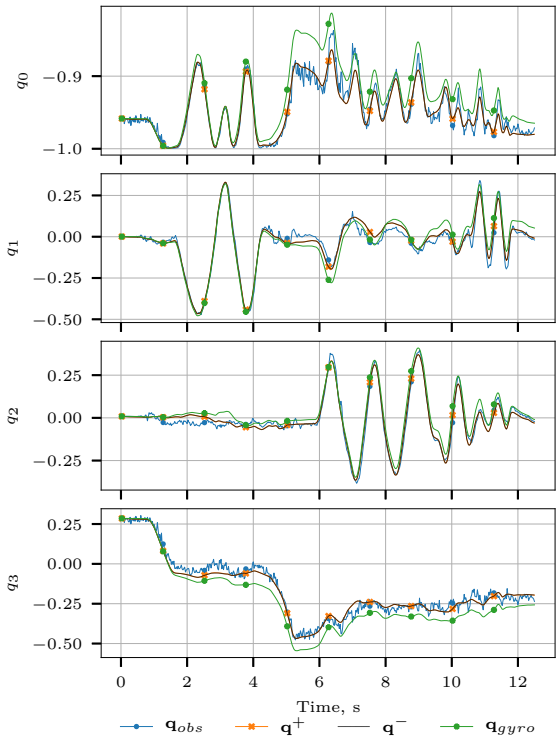

Figure 8: $\mathbf{q}_{obs}$, $\mathbf{q}^+$, $\mathbf{q}^-$ and $\mathbf{q}_{gyro}$ quaternion components. $\mathbf{q}^+$ was estimated online. $\mathbf{q}_{obs}$, $\mathbf{q}^-$ and $\mathbf{q}_{giro}$ it was constructed from the data seen in Fig. 5

Data Access

The source code of the proposed algorithm is upload on https://gitlab.com/roneydua/plataformastrapdown.git.

Acknowledgments

This study was financed in part by the Coordenação de Aperfeiçoamento de Pessoal de Nível Superior - Brasil (CAPES).

References

Baroni, L. (2017). Kalman filter for attitude determination of a CubeSat using low-cost sensors, *Computational and Applied Mathematics* **37**(S1): 72–83.

Bonnet, S., Bassompierre, C., Godin, C., Lesecq, S. and Barraud, A. (2009). Calibration methods for inertial and magnetic sensors, *Sensors and Actuators A: Physical* **156**(2): 302–311.

Castillo, P., Lozano, R., Dzu, A. E. and Dzul, A. E. (2005). *Modelling and Control of Mini-Flying Machines*, Springer-Verlag GmbH.

Espressif (2020). *ESP32 Series Datasheet*, version 3.4 edn, Espressif Systems, Shanghai, China.

Feng, K., Li, J., Zhang, X., Shen, C., Bi, Y., Zheng, T. and Liu, J. (2017). A new quaternion-based kalman filter for real-time attitude estimation using the two-step geometrically-intuitive correction algorithm, *Sensors* **17**(9): 2146.

Frosio, I., Pedersini, F. and Borghese, N. (2009). Autocalibration of MEMS accelerometers, *IEEE Transactions on Instrumentation and Measurement* **58**(6): 2034–2041.

Groves, P. D. (2015). Navigation using inertial sensors [tutorial], *IEEE Aerospace and Electronic Systems Magazine* **30**(2): 42–69.

Guennebaud, G., Jacob, B. et al. (2010). Eigen v3, http://eigen.tuxfamily.org.

Guo, S., Wu, J., Wang, Z. and Qian, J. (2017). Novel MARG-sensor orientation estimation algorithm using fast kalman filter, *Journal of Sensors* **2017**: 1–12.

InvenSense (2016). Mpu-9250 product specification, *Technical report*, InvenSense, Inc., 1197 Borregas Ave, Sunnyvale, CA 94089 U.S.A.

Kim, J., Kang, M.-S. and Park, S. (2009). Accurate modeling and robust hovering control for a quad–rotor VTOL aircraft, *Journal of Intelligent and Robotic Systems* **57**(1-4): 9–26.

Kuncar, A., Sysel, M. and Urbanek, T. (2016). Calibration of triaxial accelerometer and triaxial magnetometer for tilt compensated electronic compass, pp. 45–52.

Kuncar, A., Sysel, M. and Urbanek, T. (2017). Calibration of low-cost three axis accelerometer with differential evolution, *in* R. Silhavy, R. Senkerik, Z. Kominkova Oplatkova, Z. Prokopova and P. Silhavy (eds), *Artificial Intelligence Trends in Intelligent Systems*, Springer International Publishing, Cham, pp. 178–187.

Madgwick, S. O. H., Harrison, A. J. L. and Vaidyanathan, R. (2011). Estimation of IMU and MARG orientation using a gradient descent algorithm, *2011 IEEE International Conference on Rehabilitation Robotics*, IEEE.

Markovsky, I., Kukush, A. and Huffel, S. V. (2004). Consistent least squares fitting of ellipsoids, *Numerische Mathematik* **98**(1): 177–194.

Merayo, J. M. G., Brauer, P., Primdahl, F., Petersen, J. R. and Nielsen, O. V. (2000). Scalar calibration of vector magnetometers, *Measurement Science and Technology* **11**(2): 120–132.

Oliveira, A., Correa, D. F. and Altuna, J. (2020). Dynamic modelling and control of unmanned aerial vehicle of the quadrotor type.

Pedley, M. and Stanley, M. (2014). Magnetic calibration, *Technical report*, Freescale.

Sabatini, A. (2006). Quaternion-based extended kalman filter for determining orientation by inertial and magnetic sensing, *IEEE Transactions on Biomedical Engineering* **53**(7): 1346–1356.

Schiffler, M., Queitsch, M., Stolz, R., Chwala, A., Krech, W., Meyer, H.-G. and Kukowski, N. (2014). Calibration of SQUID vector magnetometers in full tensor gradiometry systems, *Geophysical Journal International* **198**(2): 954–964.

Spinka, O., Kroupa, S. and Hanzalek, Z. (2007). Control system for unmanned aerial vehicles, *2007 5th IEEE International Conference on Industrial Informatics*, IEEE.

Titterton, D. and Weston, J. (2004). *Strapdown Inertial Navigation Technology*, Institution of Engineering and Technology.

Valenti, R. G., Dryanovski, I. and Xiao, J. (2015). Keeping a good attitude: A quaternion–based orientation filter for imus and margs, *Sensors* **15**(8): 19302–19330.

Valenti, R. G., Dryanovski, I. and Xiao, J. (2016). A linear kalman filter for MARG orientation estimation using the algebraic quaternion algorithm, *IEEE Transactions on Instrumentation and Measurement* **65**(2): 467–481.

Voos, H. (2006). Nonlinear state-dependent riccati equation control of a quadrotor UAV, *2006 IEEE Conference on Computer Aided Control System Design, 2006 IEEE International Conference on Control Applications, 2006 IEEE International Symposium on Intelligent Control*, IEEE.

Won, S. P. and Golnaraghi, F. (2010). A triaxial accelerometer calibration method using a mathematical model, *IEEE Transactions on Instrumentation and Measurement* **59**(8): 2144–2153.

Zhong, Y., Xu, Y., He, N. and Yu, X. (2018). A new drone accelerometer calibration method, *2018 37th Chinese Control Conference (CCC)*, IEEE.